WFIRST Coronagraph Milestone 6 Final Report: Low Order Wavefront Sensing and Control

Fang Shi, Kunjithapatham Balasubramanian, Randall Bartos, Randall Hein, Brian Kern, John Krist, Raymond Lam, Douglas Moore, James Moore, Keith Patterson, Ilya Poberezhskiy, Joel Shields, Erkin Sidick, Hong Tang, Tuan Truong, Kent Wallace, Xu Wang, and Dan Wilson

Jet Propulsion Laboratory, California Institute of Technology
4800 Oak Grove Drive, Pasadena, USA, CA 91009, USA

1 OVERVIEW

In February 2014, the WFIRST-AFTA mission study, National Aeronautics and Space Administration (NASA) Headquarters, and the coronagraph Technical Analysis Committee (TAC) agreed on 9 coronagraph technology development milestones to track the maturation WFIRST coronagraph technology to Technology Readiness Level (TRL) 5. Coronagraph milestone #6 was defined as:

Low Order Wavefront Sensing and Control (LOWFS/C) subsystem provides pointing jitter sensing better than 0.4 mas rms per axis and meets pointing and low order wavefront drift control requirements.

In this report, we describe the WFIRST Coronagraph LOWFS function, its design, modeled performance, and experimental results that show that the LOWFS/C subsystem not only can sense pointing errors better than 0.2 mas but has also experimentally demonstrated closed loop pointing error suppression with residuals better than 0.4 mas rms per axis for the vast majority of observatory reaction wheel speeds.

These results were originally presented to the TAC on September 29th, 2015, concurrently with the results of WFIRST-AFTA CGI Milestone 5. The report is structured as follows. The expected WFIRST on-orbit environment and LOWFS/C performance objectives are described in Section 2. LOWFS/C design and performance modeling are presented in Section 3. LOWFS/C testbed hardware and the results of testing performed to characterize LOWFS/C performance, with emphasis on pointing error sensing and correction, are reviewed in Section 4. Section 5 summarizes the coronagraph LOWFS/C status and future work.

2 WFIRST ON-ORBIT ENVIRONMENT AND LOWFS/C PERFORMANCE OBJECTIVES

Wide-Field InfraRed Survey Telescope (WFIRST) mission concept includes the first high contrast stellar coronagraph in space intended for imaging, discovery, and spectral characterization of Jupiter, Neptune, and possibly super-Earth sized exoplanets, as well as debris discs. One of the challenges to the coronagraph performance comes from the tight requirement on the WFIRST observatory optical wavefront stability necessary to achieve the required level of starlight suppression and the stability of coronagraph contrast. The wavefront dynamics presented to the coronagraph consists of wavefront errors (WFE) in both the line-of-sight (wavefront tilt) and low order wavefront aberrations such as focus, astigmatism, and coma. Depending on the disturbance sources, these wavefront errors contain both low and high temporal frequency components, with the low frequency (sub Hz) WFE coming mostly from thermal load variation, and high frequency WFE from the vibration disturbances such as the reaction wheel assemblies (RWA) used for WFIRST-AFTA telescope pointing.

Figure 1 shows the jitter at the first focus of the coronagraph from the worst impact wheel predicted by the "Cycle 5" WFIRST observatory model [1]. This result includes the Model Uncertainty Factor (MUF) that was a function of temporal frequency and with magnitude typical for the project pre-formulation phase. Besides the high frequency LoS jitter from the reaction wheels, the telescope also suffers a slow (< 2 Hz) LoS drift caused by the telescope attitude control system (ACS) pointing error. The PSD of the LoS drift from the ACS is also plotted in Fig. 1. The WFIRST-AFTA ACS requirement allows the telescope pointing drift of up to 14 milli-arcsec rms per axis. If left uncorrected, the WFIRST LoS jitter and drift would severely degrade the coronagraph's performance, since the coronagraphs are designed to deliver the required science assuming the residual LoS error between 0.4 milli-arcsec rms per axis and 1.6 milli-arcsec, as shown in Table 1.

Table 1. The impact of residual RMS jitter values on the OMC coronagraph science yield (550 nm imaging channel).

RMS jitter (mas)	post-processing factor (fpp)	# RV planets detected by HLC in <1 day each	# RV planets detected by SPC in <1 day each
1.6	10	13	11
0.8	10	14	13
0.4	10	14	14
1.6	30	14	15
0.8	30	15	15
0.4	30	15	15
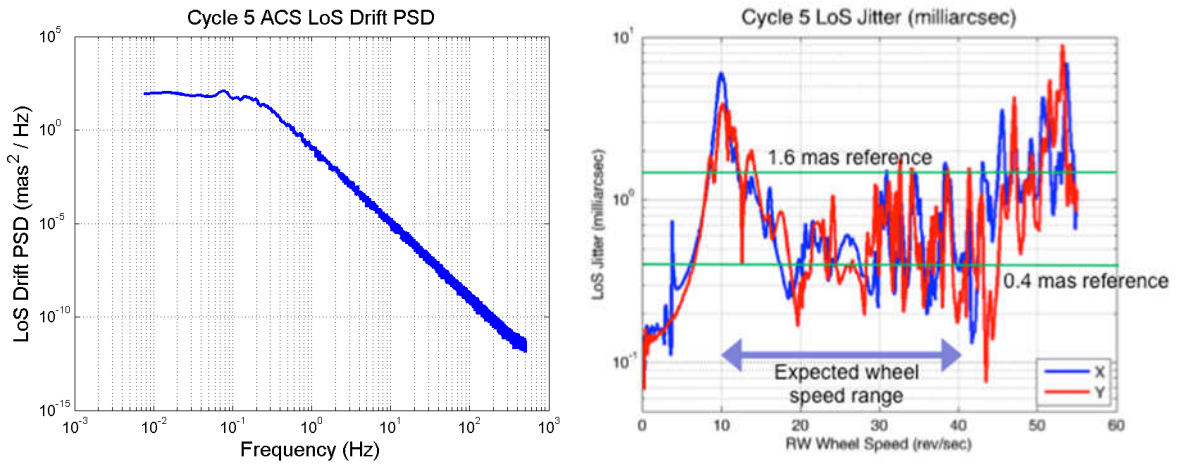
Fig. 1 LoS drift and jitter predicted from the observatory dynamic model (Cycle 5) and evaluated at the first focus of the WFIRST Coronagraph. The single axis PSD of the LoS drift from ACS is plotted on the left and total RMS drift is about 4 mas although the requirement allows the drift to be as large as 14 mas per axis. The X and Y direction jitters are plotted against the reaction wheel (RW) speed on the right. During the observation the RW speed slowly changes, ramping up from 10 to 40 rev/sec over ~18 hours. At each wheel speed the jitter contains multiple harmonic frequencies besides the fundamental frequency that equals the wheel speed.

During the coronagraph observation, the spacecraft orbiting or telescope pointing will change the solar thermal load, which will in turn cause the telescope optics surface figures and positions to change. Figure 2 shows the model-predicted thermally-induced WFE during a notional coronagraph observation scenario that lasts 56 hours [2]. From the plot we can see that the dominant portion of the thermally-induced WFE are focus, astigmatisms, and comas, caused by the telescope optics position shifts from the thermal load variations. Higher aberration modes beyond spherical are all negligibly small, in single digit picometer. It is also evident that the wavefront drift is very slow compared to LoS jitter, typically under 0.001 Hz.
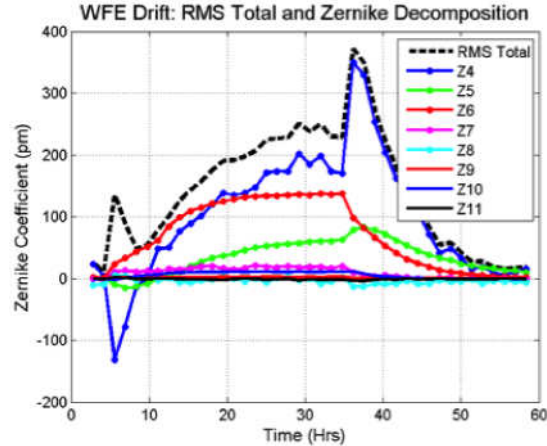
Fig. 2 WFIRST-AFTA thermally-induced wavefront error from a typical coronagraph observation scenario. The plot shows both the total RMS WFE drift as well as the decomposed major Zernike components (Z4 – Z11) of the same WFE drift. Wavefront tilt is not included in the WFE shown here.

For most optical systems wavefront drift less than 0.5 nm RMS is insignificant. However, a high contrast coronagraph is very sensitive to the wavefront error [3]. For WFIRST Coronagraph the science requires the coronagraph to have raw contrast better than 10^{-8}. Furthermore, in order to differentiate planets from residual speckles in the dark hole and to detect a planet with proper signal-to-noise ratio, the coronagraph contrast needs to be stable at a level on the order of 10^{-10} during the observation. This contrast stability requirement drives a very tight tolerance for the wavefront drift. That means that the most sensitive aberration modes, such as spherical, coma, and trefoil, need to be stable at a few 10s of picometer in order to maintain the contrast stability of $\sim 10^{-10}$. Therefore these wavefront drift errors must be measured and corrected by the LOWFS/C subsystem. From the coronagraph performance requirements, the LOWFS/C's sensor is designed to have LoS sensitivity <0.4 milli-arcsec and low order wavefront, focus (Z4) to spherical (Z11), sensitivity on the order of 10 pm.

The last considered on-orbit dynamic disturbance was the wavefront jitter – the variation of wavefront error terms above tip/tilt with temporal frequencies exceeding 2 Hz. The values of the wavefront jitter presented to the coronagraph were again taken from the "Cycle 5" dynamic model that includes appropriate MUFs. The dominate aberrations in these RWA induced wavefront jitter are of the low order mode aberrations such as focus, astigmatism and coma. Figure 3a shows the major decomposed wavefront jitter from the Cycle 5 modeling. The impact of the WF jitter on coronagraph contrast was evaluated and plotted as a function of the working angle in Fig. 3b and Fig. 3c. Since the contribution of the coronagraph jitter to contrast is below the contrast stability floor needed to image 10^{-9} contrast planet, it was concluded that this term does not need to be accurately measured or controlled by the LOWFS/C subsystem to meet the coronagraph performance.
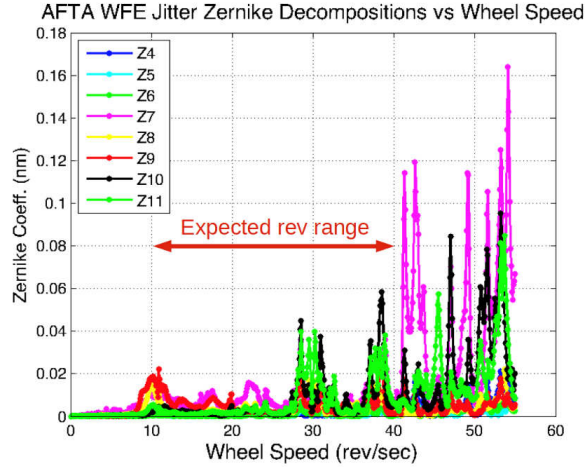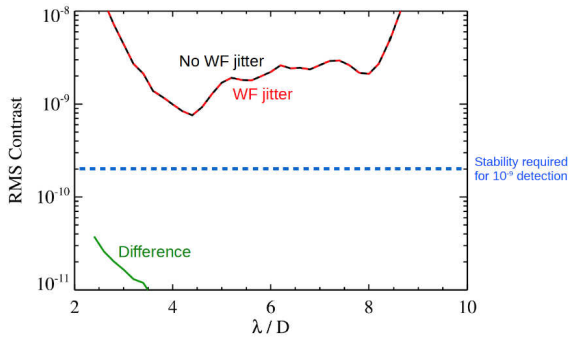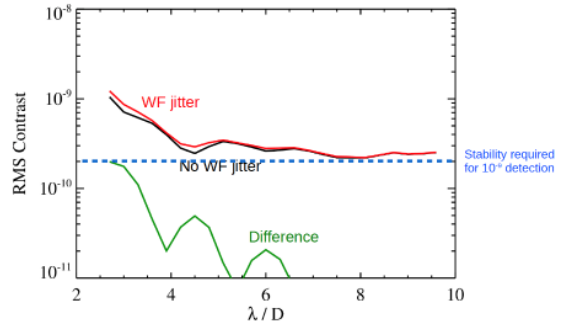
Fig. 3 Top plot (a): The "Cycle 5" model predicted wavefront jitter decomposed into the major contribution Zernike terms. Lower plots (b and c): The impact of "Cycle 5" model predicted wavefront jitter on the OMC coronagraphic contrast: (b) HLC mode and (c) SPC mode.

Finally, it should be noted that the WFIRST Coronagraph LOWFS/C subsystem works cohesively with the coronagraph's high order wavefront sensing and control (HOWS/C) subsystem, which is responsible for starlight suppression using the coronagraph's two 48x48 actuator deformable mirrors (DMs) [4]. The LOWFS/C does not set the wavefront; instead it maintains the wavefront set by HOWS/C. In other words, the LOWFS/C is a relative wavefront sensing and control sub-system.

3 WFIRST CORONAGRAPH LOWFS/C DESIGN AND PERFORMANCE ANALYSIS

3.1 Zernike wavefront sensor concept

The Zernike wavefront sensor (ZWFS) is based on the Zernike phase-contrast concept [5, 6]. Figure 3 illustrates the concept of the Zernike wavefront sensor in the context of an astronomical instrument. The electric field at the entrance pupil is given by,

$$E(u,v) = P(u,v) \cdot A\big(1 + \varepsilon(u,v)\big) \cdot e^{i\varphi(u,v)} \approx P(u,v) \cdot A\big(1 + \varepsilon(u,v) + i\varphi(u,v)\big) \tag{1}$$
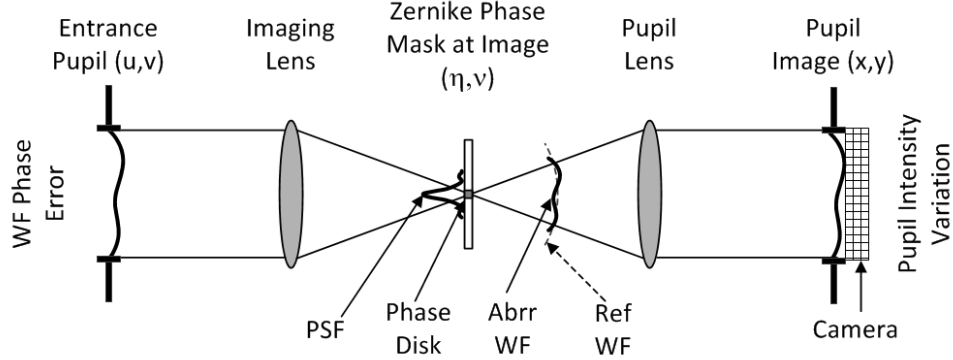
Fig. 3 Illustration of Zernike wavefront sensor concept. Lenses are used to represent the optics between the entrance pupil, the imaging plane, and the re-imaged pupil plane. The Cartesian coordinates of these planes are also labeled.

where $P(u,v)$ is the pupil amplitude support function, which describes the pupil geometry, A is the mean electric field amplitude, $\varepsilon(u,v)$ is the amplitude variation across the entrance pupil, and $\varphi(u,v)$ is the phase variation across the pupil, which is the wavefront error. The light from telescope is focused at the image plane, where a phase disk of size $\sim\lambda/D$ introduces a phase change of $\pi/2$ to the center potion of the PSF and forms a reference wavefront. The reference WF interferes with the light passing outside the phase disk which contains wavefront error. When imaged again to a pupil plane the interference turns the phase variation at the entrance pupil to the linear intensity variation in pupil image [7],

$$I(x,y) \approx A^2 \cdot \big(1 + \varepsilon^2(x,y) + 2\varphi(x,y)\big) \tag{2}$$

In WFIRST Coronagraph the role of LOWFS/C is to maintain the wavefront set by the HOWFS/C, which creates the coronagraph's dark hole at the beginning of a coronagraphic observation. The WFIRST LOWFS/C's ZWFS therefore works in the relative wavefront measurement mode, sensing the wavefront changes from the reference point set by HOWFS/C instead of measuring the absolute wavefront. Because of this and the fact that the wavefront drift during the WFIRST coronagraph observation is small, typically less than 1 nm RMS, we construct a differential image based linear algorithm to compute the relative wavefront error directly from the pupil image intensity. The differential images between the aberrated ZWFS image I_{abbr} and reference ZWFS image I_{ref} taken right after the HOWFS/C can then be used to derive the wavefront error changes $\Delta\varphi$ needed for LOWFS/C,

$$\Delta\varphi = \left(\frac{I_{abbr} - I_{ref}}{2A^2}\right) = \frac{\Delta I}{2A^2} \tag{3}$$

3.2 LOWFS/C for WFIRST-AFTA Coronagraph

WFIRST Coronagraph LOWFS/C wavefront sensor is designed to use the rejected starlight from coronagraph's focal plane occulting mask. The WFIRST Occulting Mask Coronagraph (OMC) is convertible between two operating modes, hybrid Lyot coronagraph (HLC) and shaped pupil coronagraph (SPC), and each configuration has its unique and complimentary science role and capability [8]. They require different focal plane masks (FPM) selected by a filter wheel. Figure 4 shows the WFIRST OMC's optical function diagram. The coronagraph light passes through 2 DMs, starlight suppression masks unique to each mode of operation, and goes to the coronagraph's science camera or

integral field spectrograph (IFS). The rejected light, which contains almost all of the starlight, reflects off the focal plane mask and is used for LOWFS/C wavefront sensing. One of the key features of WFIRST LOWFS/C design is that the Zernike wavefront sensor's phase disk is designed and fabricated directly on the reflective side of the focal plane mask. In other words, the FPM has dual functions: coronagraph starlight suppression mask in transmission and LOWFS/C Zernike WFS mask in reflection. This way the starlight rejection and wavefront sensing occur at the same location. This not only ensures that the ZWFS measures WFE where the coronagraph needs but also avoids the non-common path error on ZWFS since the light reflecting off the FPM contains both the ZWFS' reference WF and aberrated WF, and the subsequent LOWFS/C optics will be common to both. The details of ZWFS mask design are different depending on the coronagraph mode [9, 10], but they all have the ZWFS phase disk built in.

For LOWFS/C the coronagraph's FPM acts as a low-pass spatial filter because of its limited size of the reflecting area, whose diameter is ~6 λ/D for HLC or ~5 λ/D for SPC. Therefore, the LOWFS/C Zernike wavefront sensor can only sense the low order wavefront error and is insensitive to mid or high spatial frequency WFE. Fortunately, as shown in Section 1 the dominant WFIRST WFE drift is low order in nature. Currently LOWFS/C ZWFS senses the first 11 Zernike terms: tilts (Z2, Z3), focus (Z4), astigmatisms (Z5, Z6), comas (Z7, Z8), trefoils (Z9, Z10), and spherical (Z11). A fixed 20% spectral filter centered at 0.55 um is placed in front of the CCD camera. The baseline LOWFS/C camera uses the E2V's CCD39 which has 80x80 pixels, 4 parallel readout ports, and a built-in TEC cooler which has a low readout noise of 4e- and high frame rate of 1 kHz. The ZWFS image is read out and processed by a real time computer. The wavefront error, in the form of 10 Zernike coefficients (Z2-Z11), is computed at camera red out rate of 1 kHz.
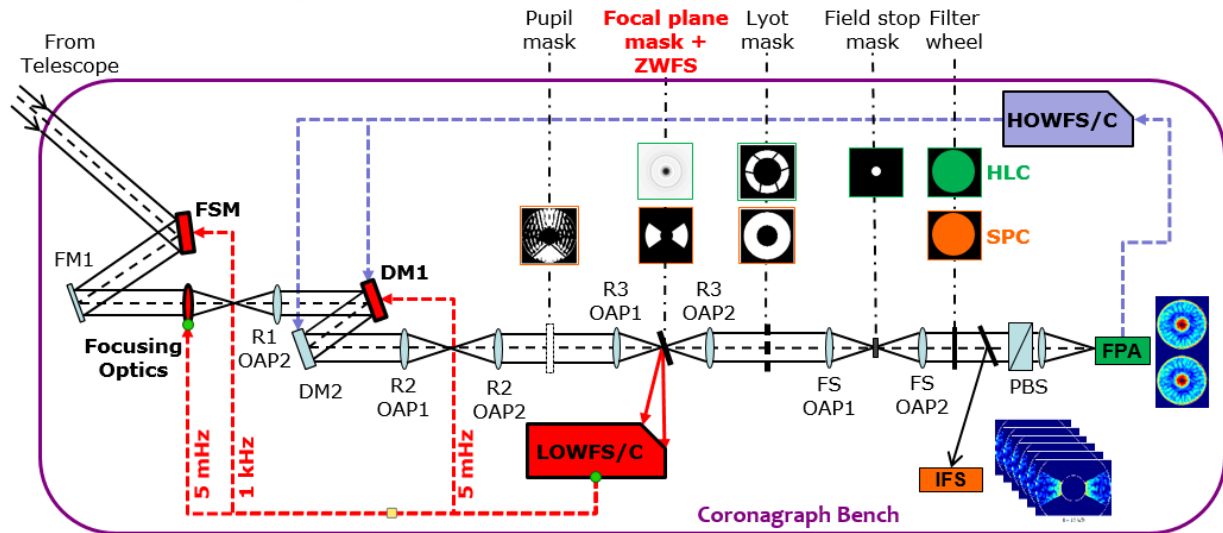
Fig. 4 Functional illustration of WFIRST Coronagraph instrument (CGI) bench. Starlight from the telescope and relay optics enters CGI bench at left through the fast steering mirror (FSM). Two deformable mirrors (DM1 and DM2) correct the wavefront phase and amplitude for high contrast imaging. Relay optics are off-axis parabolas (OAP). The WFIRST CGI can operate in either HLC or SPC mode with Hybrid Lyot Coronagraph masks (top row) and Shaped Pupil Coronagraph masks (bottom row) being able to be switched in via filter wheels at pupil or image planes, indicated with dot-dashed lines in the figure. A selectable mirror sends coronagraph light to either the imaging camera (FPA) behind a polarizing beam splitter (PBS) or the integral field spectrograph (IFS). The rejected starlight from the focal plane mask, which has the LOWFS/C phase mask built-in, is captured by the LOWFS/C lenses and sent to LOWFS/C camera. The LOWFS/C subsystem, indicated by the thicker lined components and thicker dash lines, controls FSM, Focusing Optics, and DM1 with different updating speeds as labeled in their corresponding signal paths.

The ZWFS sensed WFE is used to control corresponding wavefront correctors by the LOWFS/C, as shown in Fig 4. The sensed tip-tilt (Z2, Z3) is used to drive the Fast Steering Mirror (FSM) control loop with command update rate of 1 kHz to suppress the LoS jitter and drift. Since the thermally induced WFE drift is very slow the sensed low order WFE (Z4 – Z11) can be time-averaged over long period (minutes) to reduce the sensor noise without compromising the control bandwidth. The sensed focus term (Z4) is used to control the coronagraph's focusing optics which is an actuated fold flat in a focused beam designed as a part of the coronagraph instrument. Focus is one of the dominant

mode of WFIRST WFE drifts. Correcting it with a dedicated Focusing Mirror (FM) will reduce the stroke burden on the deformable mirror. The rest of low order wavefront error terms (Z5 – Z11) sensed by ZWFS are sent to DM1, which is conjugated to the system pupil, for the correction.

Besides LoS jitter the telescope vibration from the reaction wheels will also cause the WFE jitter with frequencies and amplitudes depending on the RW wheel speeds. The RW induced WFE jitter are dominated by a few low order modes such as focus, astigmatisms and comas [1]. For the high frequency (> 2 Hz) wavefront jitters the LOWFS/C does not have the bandwidth to suppress them. However, the modeling has shown that the impact of WFIRST WFE jitter on coronagraph contrast and contrast stability is negligible, as was discussed in Section 2. Some of the WFE jitter effect can also be removed during the coronagraph image post-processing. Furthermore from the recorded the ZWFS data we can also evaluate the uncompensated LoS and WFE jitters and use the information for data editing, discarding some science exposures in which the residual jitters are too large.

3.3 Zernike wavefront sensor modeling and performance analysis

To analyze the performance of the Zernike wavefront sensor, a diffraction model has been developed which includes WFIRST-AFTA pupil and total system optical transmission (0.24), HLC and SPC FPMs with the built-in ZWFS phase disk, the initial wavefront from coronagraph's HOWFS/C, and the ZWFS CCD camera. Example images in Fig 5 show the ZFWS modeling process. For photometry, a GV0 star spectral is used with a 20% ZWFS spectral filter centered at 561 nm for rejected starlight and the star magnitude varies from $M_V = 0$ to $M_V = 8$. The pupil sampling on the ZWFS camera is 16x16 pixels, which has been chosen to ourad to asecptimize the sensor signal-to-noise ratio (SNR) and minimize WFE modes cross-talk. The detector model is based on the E2V CCD39 chip with 4 e- read out noise, 1 e- dark noise at 1 kHz frame rate, and 80% to 87% quantum efficiency (QE) across the spectral band of ZWFS.
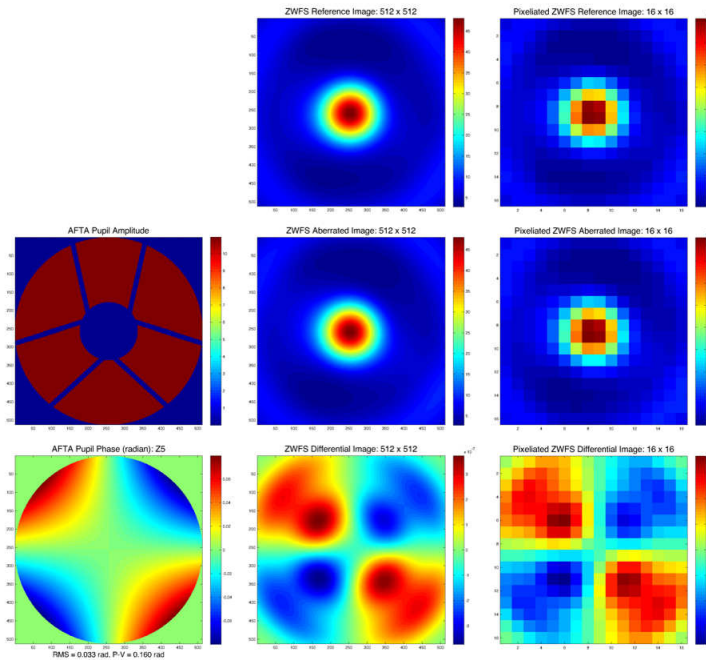
Fig. 5 Example images of ZWFS modeling process using the HLC/ZWFS focal plane mask. The images on the left column are the amplitude and phase error at WFIRST-AFTA entrance pupil. Here the phase error is 3 nm (RMS) astigmatism (Z5). The images in middle column are, from top to bottom, the high resolution ZWFS reference (no phase error) image, the aberrated image corresponding to 3 nm of Z5, and the differential image between the aberrated and reference image. The images on the right are, from top to bottom, the corresponding pixelated (16x16 pixels) reference, aberrated, and differential images. The differential images resemble the phase error input and the pixelated differential image (lower right) is the signal for ZWFS sensing.

Using the ZWFS model we have studied the performance of ZWFS against various parameters such as the star magnitude, detector noise, sensor spectral bandwidth, ZWFS phase disk diameter and depth. One of the important ZWFS performance metrics is the ZWFS's noise equivalent sensing error. It measures how the sensor performs when the photon and detector noise are present. Figure 6 shows the noise equivalent LoS angle and noise equivalent sensing error for three ZWFS configurations. From the plots we can see that the ZWFS noise equivalent sensing error is dominated by the photon noise with sensing errors and star magnitudes following the simple power law. Only for fainter stars of $M_V > 7$, the noise curves begin to deviate from this power law, indicating that the detector noise becomes more significant. It is important to emphasize that these noise curve are evaluated at camera readout rate of 1 kHz, i.e. at exposure of 1 msec. For slowly drifting low order WFE the sensor can gain much performance through image averaging over longer period of time which is equivalent to increasing the stellar brightness. For example, if we average camera images for 1 minute, the equivalent exposure time increases by a factor of 60,000, then the equivalent stellar magnitude gain is $\Delta M_V \approx -12$. The 4 nm sensing error from an $M_V = 5$ star for HLC ZWFS will be reduced to 16 pm. More details on the ZWFS modeling and analysis results can be found in Ref [11].
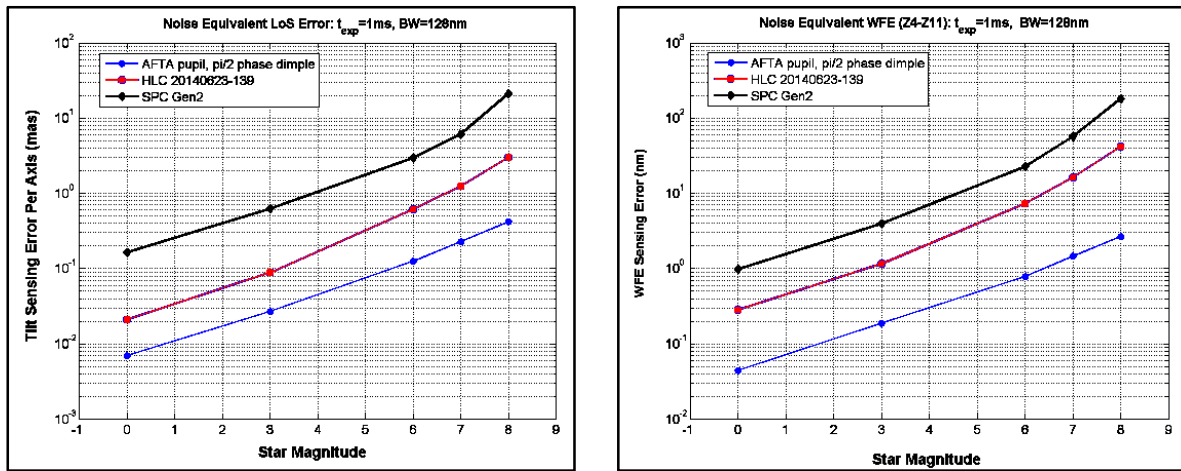
Fig. 6 ZWFS noise performance for a simple Zernike phase disk, HLC, and SPC configurations with the ZWFS camera running at 1 kHz frame rate. The plot on the left is the noise equivalent angle (on-sky) and plot on the right is that of noise equivalent low order wavefront sensing error. PSF differences caused by either diffraction (for the case of SPC) or wavefront (for the case of HLC) increases the ZWFS sensing error compared with an ideal PSF on ZWFS with a simple phase disk.

3.4 Line of sight control loop design and performance analysis

A schematic overview of the LoS control loop is shown in Fig 7. There are two control branches. A feedback path is used for compensation of the slow ACS drift. The controller in this branch is designed to reject high frequency sensor noise. Loop shaping is used to enhance performance. The second path is targeted to feed the high frequency tonal information forward to the FSM. Recursive least squares fitting of the tones using RWA wheel speed information was implemented to suppress these tones excited by the RWAs [13].

LoS Feedforward   LoS Feedback Loop
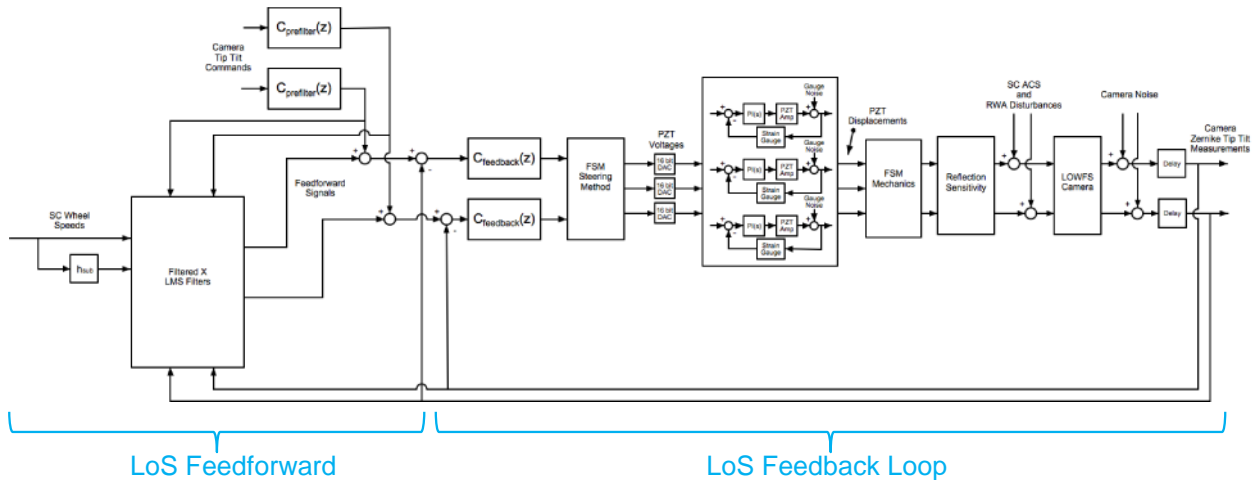
Fig. 7. Block diagram depiction of the implemented line-of-sight drift and jitter compensation loops using a Fast Steering Mirror (FSM). The LoS control contains both a feedback loop and a feedforward loop. The feedback loop bandwidth is tuned to reduce the sensor noise and provide control bandwidth to correct the slow LoS drift from ACS. The feedforward loop uses the knowledge of RWA wheel speed from ACS telemetry, dynamic model identified harmonic frequencies together with LOWFS sensor to cancel the RWA wheel induced the LoS jitter.

The line-of-sight control uses the Fast Steering Mirror (FSM) with three PZT actuators, which is inherited from the SIM project [12]. The FSM PZT actuators have strain gauge sensors that are used to close a local loop around the PZT displacements. This loop linearizes the hysteresis of the PZTs, cancels drift due to creep, and achieves a bandwidth of 150 Hz.

Figure 8 and Table 1 summarize the modeled FSM loop performance against the WFIRST reaction wheel induced jitter shown in Fig 1. In this model we used the ZWFS sensor noise model for HLC configuration shown in Fig. 6, as well as the measured FSM driver noise. Table 1 shows the fraction of time over which the residual jitter meets three coronagraph performance evaluation criteria, assuming that the wheel speed is uniformly distributed from 10 to 40 rev/sec.
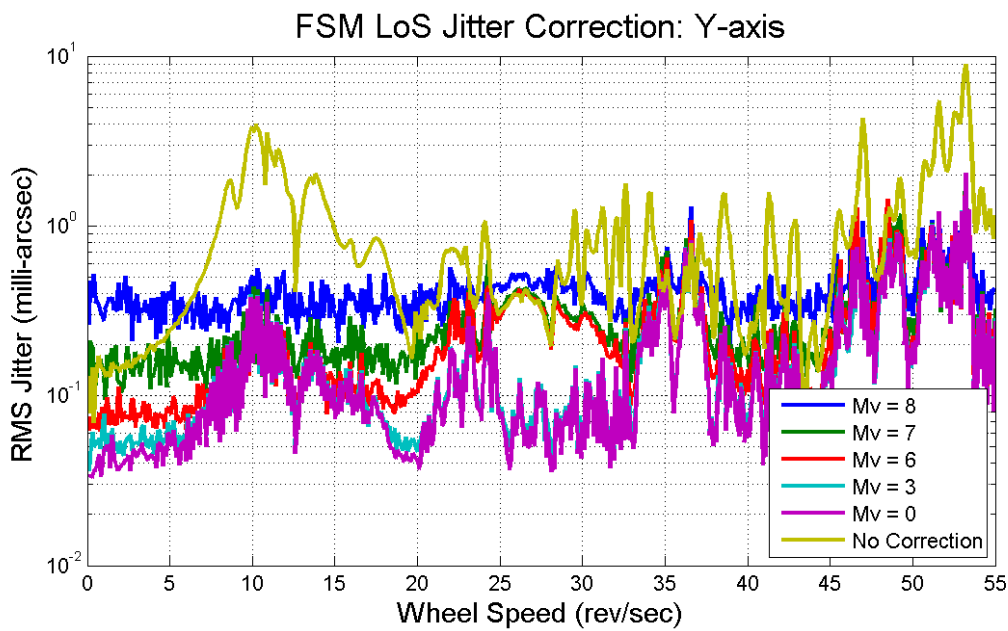
Fig. 8 WFIRST jitter input and the residual LoS jitter with the LOWFS/C FSM loop plotted against the RW wheel speed. The plot shows the Y axis LoS jitter. Lines of different colors represent the residual jitter of different stellar magnitudes, which affect the ZWFS sensor noise. *The results for Mᵥ = 6 are from the recent updated servo which has the loops better tuned to reduce the impact of the sensor noise. The tuning has improved the percentage of time for residual jitter, for example for the case of ≤0.4 mas from 83% to 94% in X and 93% to 95% in Y. The curves in Fig. 8, however, are still showing the results before the servo update.

Table 2. Percentage of time the residual jitters meet the three coronagraph performance evaluation criteria.

Star magnitude (Mᵥ) / Jitter (milliarcsec)	X jitter residual over 10 - 40 rev/sec			Y jitter residual over 10 - 40 rev/sec		
	≤ 0.4	≤ 0.8	≤ 1.6	≤ 0.4	≤ 0.8	≤ 1.6
0	95%	98%	100%	97%	100%	100%
3	95%	98%	100%	97%	100%	100%
6*	94%	100%	100%	95%	98%	100%
7	83%	98%	100%	91%	99%	100%
8	59%	97%	100%	52%	99%	100%

3.5 Low order WFE control with the deformable mirror

The WFIRST LOWFS/C uses the coronagraph's DM1 to correct sensed low order wavefront drift Z5 to Z11. The deformable mirror actuator height versus control voltage curve of each actuator is nonlinear and these curves are slightly different for each actuator. Each DM actuator's gain will be calibrated around its bias voltage, but some calibration error is inevitable. We carried out an investigation to determine how tight the requirements on DM actuator gain knowledge have to be in order to use the DM for correcting low order WFE terms above focus without unacceptably degrading the coronagraph contrast. To understand the impact of such actuator gain-errors on the LOWFS/C, we introduced two types of actuator gain-error factors: the static gain-error factors of $\vec{\delta}_s$ and time-varying or dynamic gain-error factors of $\vec{\delta}_{d_i}$, that is,

$$\vec{u}_{g_i} = \vec{u}_{DM_i}\left(1 + \vec{\delta}_s\right)\left(1 + \vec{\delta}_{d_i}\right) \tag{4}$$

where $\vec{u}_{DM_i}$ is the desired LOWFS/C DM commands for the current iteration DM control (denoted by subscript *i*) and $\vec{u}_{g_i}$ is the actual DM poke the actuator realized, which includes the DM actuator gain error factors.
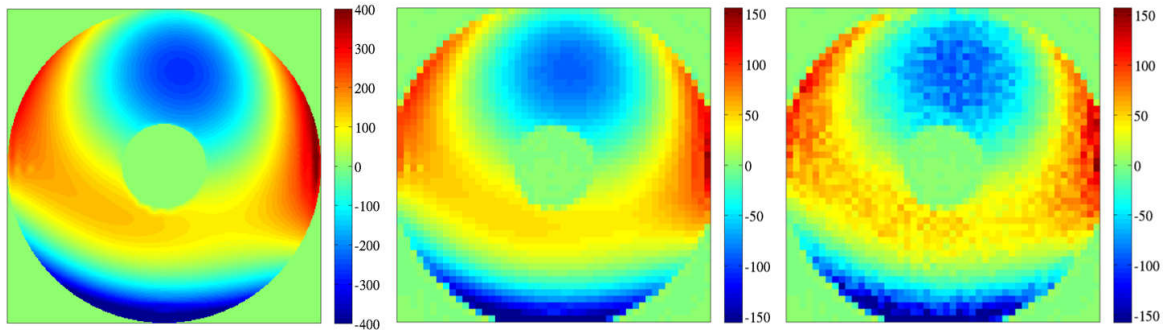
Fig. 9 Example of DM actuator height map with and without the DM gain calibration error. In this example the DM is trying to compensate the WFE error from the WFIRST-AFTA telescope drift, which is the OPD map on the left. The sign of OPD is flipped in this plot for easy comparison with the DM height maps. On the DM actuator height maps (middle and right plots) each pixel represents the height of an actuator in the 48x48 actuator DM. The DM actuator height map in the middle is from DM control without DM gain calibration error while the actuator height map on the right is from the DM with actuator gain calibration error of $\vec{\delta}_s = 20\%$ and $\vec{\delta}_{d_i} = 10\%$.

Figure 9 illustrates the effect of the DM gain calibration error. It shows that the DM gain calibration error will cause post LOWFS/C correction residual WFE to fall into mid to high spatial frequency because the DM actuator gain calibration error is, in general, random among the actuators. The LOWFS/C sensor, however, will not able to sense these mid to high spatial frequency DM residual error due to its limitation in spatial resolution. Therefore using a deformable mirror to correct the low order WFE commanded by the LOWFS/C may adversely affect the coronagraph's performance because these mid to high spatial frequency WFE will cause extra speckles in the coronagraph dark field and degrade the coronagraph contrast.

We use the LOWFS/C model to simulate the LOWFS/C closed loop sensing and control using DM1 for the thermally induced WFIRST WF drift shown in Fig. 2. Figure 10 plots the RMS contrast difference with different DM actuator gain errors when the DM is used to correct the same thermal drift shown in Fig 2. In this simulation the LOWFS/C sensing error is v small, by using an $M_V=5$ star and integration time of 1000 sec, so we can compare only the DM gain error effect. From Fig. 10 we can see that for a typical WFIRST WFE drift if we wish to maintain the contrast stability to ~10^{-10} level we need to calibrate the DM actuator gain to better than 10% ($\vec{\delta}_s = 0.1$). Furthermore because in our model we have defined the DM gain error as the proportional terms to the DM stroke (Eq. 4), if the WFE drift is larger the DM calibration requirement will be even tighter. Otherwise we would have to rely on the "data editing" to discard the coronagraph science data when the WFE drift is too large. More details on LOWFS/C DM gain error analysis can be found Ref [14].
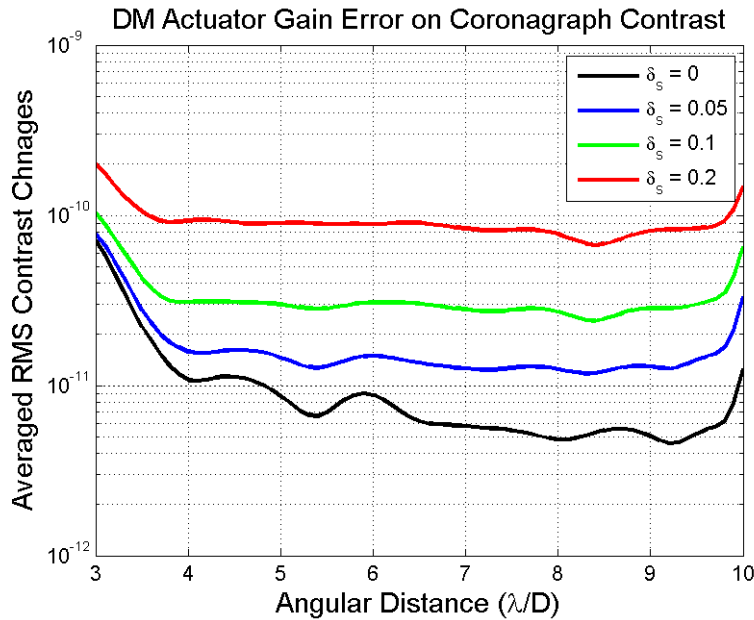
Fig. 10. RMS contrast averaged across the WFIRST-AFTA observation time span. Each differential contrast map is equal to a contrast map at a time-step minus the nominal. The individual RMS change computed over azimuth was obtained first, then averaged over all of the time steps. Finally it is plotted versus field radius. The curves represents different DM actuator statics gain errors, from ideal ($\delta_S = 0\%$) to $\delta_S = 20\%$ while the dynamic gain errors is set to be ½ of the static gain errors.

4   LOWFS/C TESTBED DESIGN AND EXPERIMENTAL RESULTS

4.1   Optical Telescope Assembly Simulator and LOWFS/C Testbed

To evaluate the performance of the stand-alone LOWFS/C subsystem and later the complete coronagraphic system in the representative WFIRST dynamic environment we have designed and built an Optical Telescope Assembly (OTA)

Simulator. The OTA Simulator acts as the testbed star source, providing point source light with adjustable brightness and spectral bandwidth. It also creates the pupil shape that mimics the obscured 2.4 meter WFIRST-AFTA telescope. Finally, this unit injects the expected on-orbit WFIRST wavefront drift and LoS jitter into the OMC coronagraph testbed. Besides the OTA Simulator sub-bench, the LOWFS/C testbed used to demonstrate Milestone 6 consisted of the Zernike wavefront sensor (ZWFS) with a commercial CCD camera running at 1000 Hz frame rate, the Fast Steering Mirror (FSM) for LoS jitter correction, and the focusing mirror (FM). Figure 11 and its caption describe the optical layout and functions of the OTA Simulator and LOWFS/C testbed.

The OTA Simulator relies on the precision linear movement of the powered optics (telescope, SM, OAP2) to generate small (sub-nm) low order wavefront error. Pure low order aberration modes such as focus, coma, astigmatism, and spherical can be generated by properly moving the powered optical mirrors. To accurately move the powered optics we use PZT actuators with strain gauges which can provide microns of motion with sub nm precision and linearity better than 0.2%. In the Milestone 6 tests we tested a Hybrid Lyot Coronagraph focal plane mask which has the Zernike WFS phase disk built in, as shown in Fig. 12. This was deemed to be the more challenging case compared to Shaped Pupil occulter, as the HLC occulter center is used both for coronagraph in transmission and LOWFS in reflections. SPC occulter presents a simpler case, as the coronagraph and LOWFS regions are spatially separated on the mask and thus the design can be independently optimized for the two functions. Both HLC/LOWFS and SPC/LOWFS occulting masks are fabricated with high accuracy and yield at JPL's MicroDevices Lab.
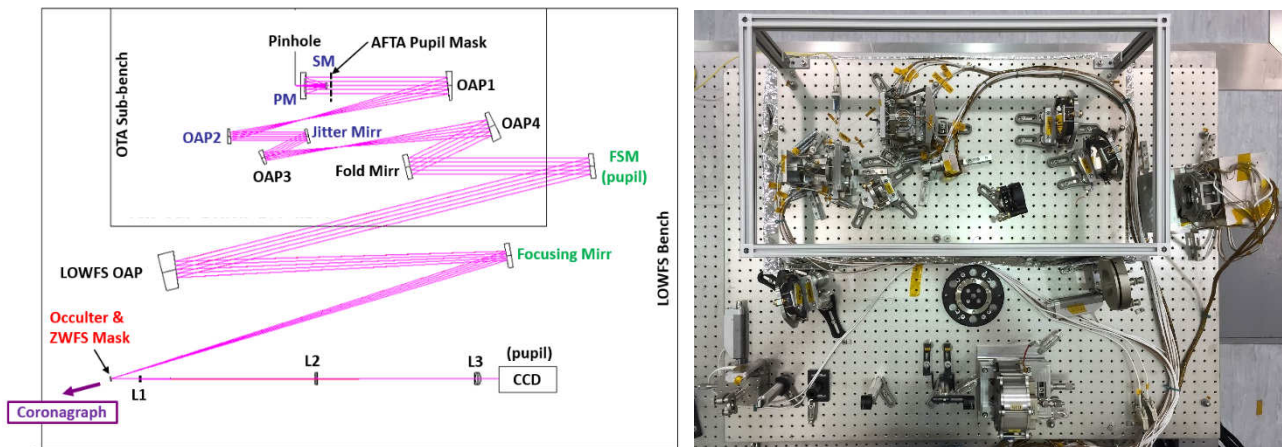
Fig. 11 The OTA Simulator and the LOWFS/C testbed. The plot on the left is the optical layout and picture on the right is the testbed after integration, oriented the same way as the optical layout on the left. The OTA Simulator uses a fiber illuminated pinhole as the star. The light from the pinhole is collimated by a miniature telescope with the scaled down WFIRST-AFTA telescope primary mirror (PM) and secondary mirror (SM). A pupil mask behind the secondary mirror support creates the WFIRST-AFTA pupil shape which has the SM obscuration and the shadows of the SM supporting struts. This pupil is then relayed by a pair of OAPs (OAP 1 and 2) to the Jitter Mirror (JM) which is a small flat mirror on a PZT tilt stage with strain gauges. It is used to inject the high frequency LoS jitter into the system. After the JM another pair of OAPs (OAP 3 and 4) create a collimated beam and form another pupil just outside the OTA Simulator sub-bench for interface with the testbed interface optics, which, on the LOWFS/C testbed, is the FSM. In OTA Simulator the miniature AFTA telescope, SM, and OAP2 are all actuated in 6 degrees of freedoms by PZT actuators to create the needed low order WFE modes that simulate the WFIRST-AFTA WFE drift. The LOWFS/C testbed starts with the FSM. The following LOWFS OAP focuses beam on the ZWFS mask. The beam is folded by a flat mirror on a linear stage acting as the focus correcting mirror. The ZWFS light reflects from a focal plane mask and is collected and collimated by Lens 1 and re-imaged to LOWFS/C CCD camera by Lens 2 & 3. They form a pupil image of 16x16 pixels on the LOWFS/C CCD camera.
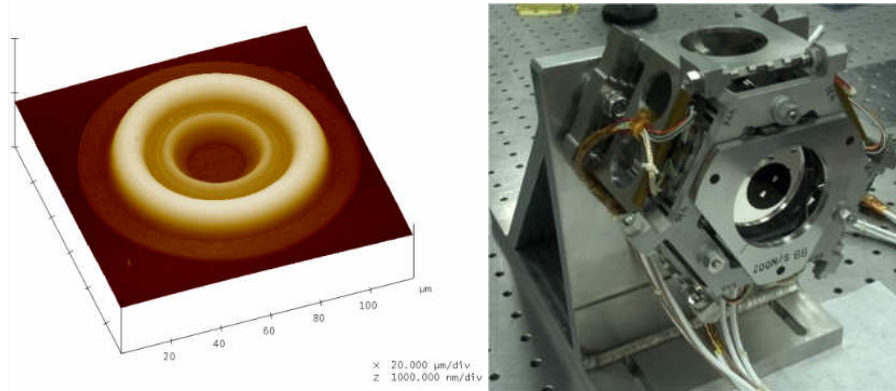
Fig. 12. Key hardware components: at Left is the atomic force microscope scan of Hybrid Lyot Coronagraph / LOWFS focal plane occulting mask. A reflective metal disc deposited on a glass substrate and a transparent dielectric layer on top of the metal form the occulter. The design was optimized for high coronagraph performance in transmission and adequate ZWFS performance in reflection. The central "dip" in the dielectic layer profile provides the Zernike wavefront sensing functionality. At right the Fast Steering Mirror (FSM) used by CGI LOWFS/C for correcting LoS error was built and flight qualified by another JPL project.
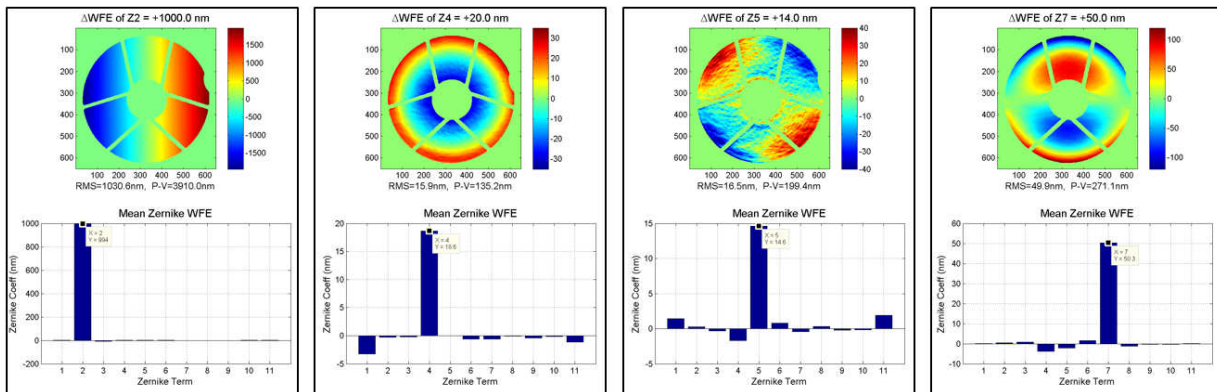
Fig. 13. Zygo interferometer measurement of the OTA Simulator generated pure aberration modes. The plots show the example aberration modes (from left to right) of tilt (Z2), focus (Z4), astigmatism (Z5), and coma (Z7) created by OTA Simulator. On top of each panel is the OPD difference between the nominal and the commanded OTA Simulator measured by the Zygo. The commanded pure mode RMS aberration is listed on top of each panel and the decomposed Zernike components RMS values are shown in the bar chart below with the RMS value of the corresponding mode labeled. Besides the mode meant to be created the bar charts also show the presence of small amount of other modes, likely from the air turbulence or testbed drift. The relative strength of these "undesired" modes becomes negligible for the strong pure modes, such as tilt and coma.

After the LOWFS/C testbed integration and alignment the OTA Simulator was calibrated using a Zygo interferometer. First, the influence function of each PZT was measured with the Zygo. They were compared with the OTA Simulator FEM modeled influence functions. The measured and modeled data have shown a very good match within the fluctuations from the lab seeing. The influence functions of all the PZTs are then used to create a control matrix which enables us to command the PZTs of OTA Simulator to create a "pure" WFE aberration mode, such as focus, astigmatism and coma. To overcome the air turbulence we use the full stroke of PZTs for some weak modes, such as astigmatism. Figure 13 shows the Zygo measurement of these pure aberration modes created by OTA Simulator. The Zygo measurements show an excellent agreement between the commanded mode and measured mode.

4.2   LOWFS/C experimental results: sensing

Sensing experiments were carries out in the LOWFS/C testbed for tip/tilt and focus errors in order to compare the ZWFS sensor accuracy to the prior OTA-S calibration results, characterize the noise performance and determine the lowest signal level that can be detected.

As the thermal environment in the LOWFS/C testbed was not actively controlled, thermally-induced testbed drifts had the potential to overwhelm small wavefront errors injected into the LOWFS/C subsystem. For this reason, temporal square wave modulation, or "chopping," of the input wavefront errors was used in the testbed to distinguish the signal from the thermal drift. This chopping can be seen in figures 14 and 15. The figures show both the noisier raw data acquired at 1kHz rate and the smoothed data. When the detector noise is smoothed out the LOWFS sensor is cleared be able to sense the LoS chopping as small as ±0.19 mas and focus error as small as 0.25 nm. Two points must be made in regards to this noise. First, the stand-alone LOWFS/C testbed used for Milestone 6 has more noise compared to the future Milestone 9 OMC testbed, as well as the flight implementation of the LOWFS/C. Several factors identified as contributing to the noise in the LOWFS testbed are summarized in Table 3 and are being addressed in the dynamic coronagraph testbed. It should also be noted that for all error terms above tip and tilt, the LOWFS/C will perform long term averaging to extract the slow-varying thermal low-order wavefront error terms. Indeed, while the LOWFS camera acquires frames at ~1000 Hz, the planned correction rate for terms above tip and tilt is only ~0.005 Hz.
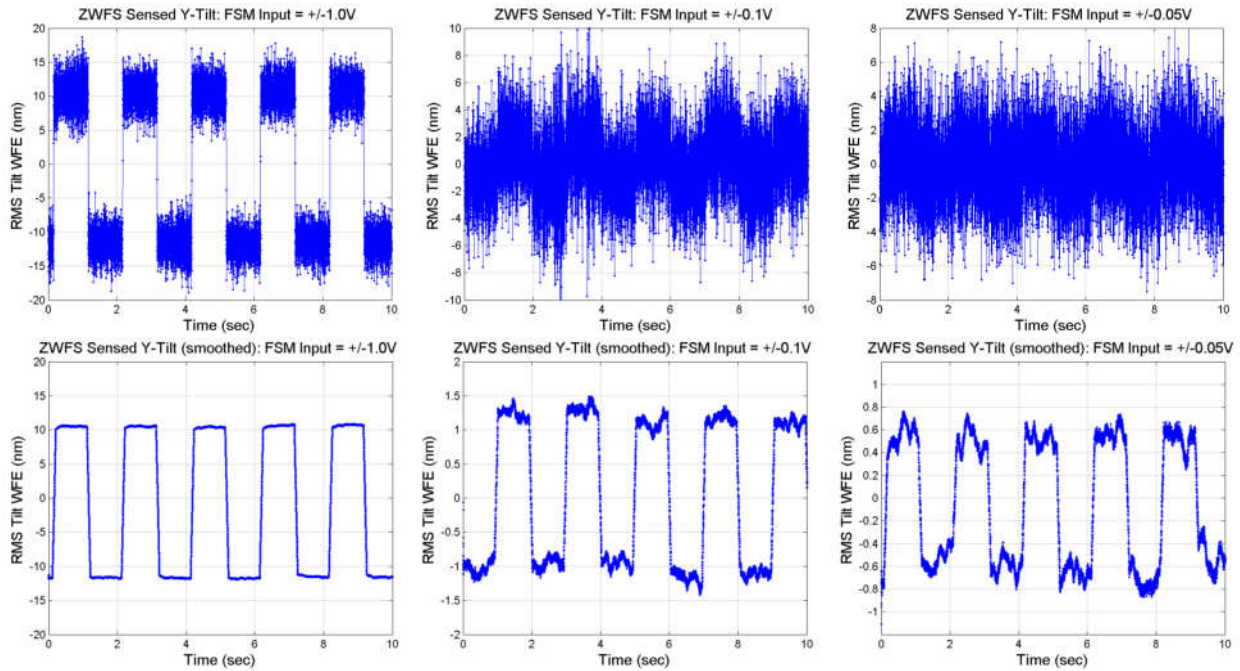
Fig. 14. ZWFS sensing of injected tilts: raw data (top row) and smoothed data (bottom row). The injected signal step was 22 nm (7.7 mas on-sky equivalent) – left column; 2.2 nm (0.77 mas on-sky equivalent) – middle column, and 1.2 nm (0.38 mas on-sky equivalent) – right column.
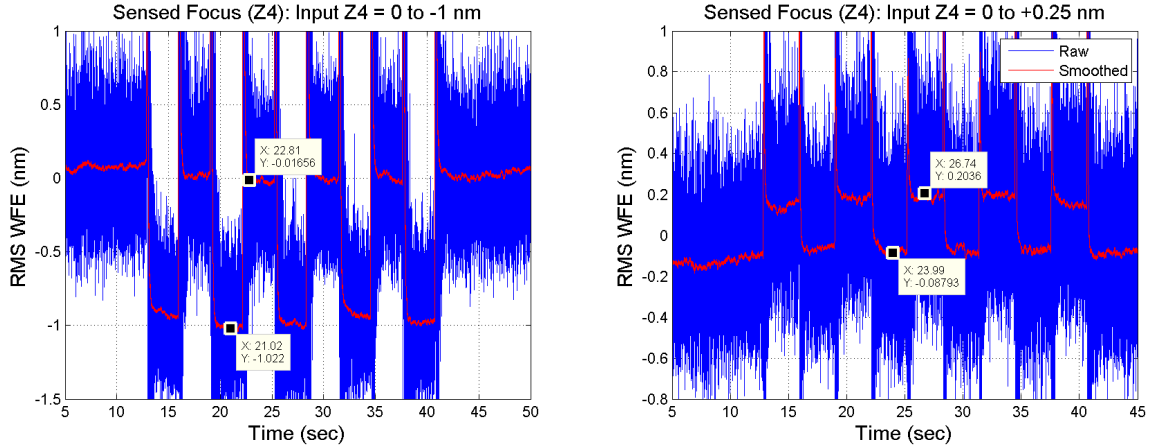
Fig. 15. ZWFS sensing of injected focus. The injected signal step was 1 nm on the left and 0.25 nm on the right. Raw and smoothed data are shown. Long term averaging will be used for sensing the focus term on orbit.

Table 3. Excess noise sources in the LOWFS/C testbed and their planned mitigation in the Milestone 9 testbed.

LOWFS/C Testbed Noise Source	Mitigation
COTS LOWFS camera read-out noise significantly exceeded vendor spec at 1 kHz readout rate (30e- vs. 6e-) due to the longer camera cable	Using low-noise sCMOS camera in the Milestone 9 testbed. Flight LOWFS camera sensor trade ongoing, several viable options exist.
COTS PZT driver line noise and transition spikes	Implemented low-noise custom electronics for controlling OTA Simulator PZT actuators for Milestone 9
High environmental noise on LOWFS/C testbed	Milestone 9 coronagraph dynamic testbed features enhanced isolation compared to the stand-alone LOWFS/C testbed.

4.3 Experimental results: line-of-sight error closed loop control

Closed loop testing of LoS error suppression was performed in the stand-alone LOWFS/C testbed using the control algorithm described in Section 3.4. The LoS disturbances introduced by the Jitter Mirror in the OTA Simulator include both the slow and fast components. For the slow LoS drift component, we used two types of inputs:

1. ACS error estimate from the Cycle 5 observatory model. The total rms error is 4 mas per axis, with almost all of the energy below 1 Hz (Fig. 1).

2. A disturbance with the same power spectral distribution as (1) but scaled up to reach the level of 14 mas per axis, which is the observatory requirement on ACS performance imposed by the wide field instrument.

For the fast (jitter) disturbance component, we used the Cycle 5 estimates for contribution from the worst reaction wheel, shown in Fig. 1. Since the jitter values vary strongly in the relevant 10 - 40 rev/sec range, we focused in our experiments on the worst case jitter values that correspond to 10 Hz and also more typical "benign" jitter values predicted at 20 Hz. Since even the worst case values predicted in Cycle 5 were below the 14 mas requirement, we also tested loop performance with single tonal disturbances scaled up to 14 mas rms per axis between 10 and 40 Hz.

Fig. 16 shows the time-domain view of the control loop performance. The LoS error plot starts with lab noise sensed by the LOWFS, while both the Jitter Mirror and the FSM are off. Then around *t = 6.8 sec* the Jitter Mirror begins to introduce the ACS and jitter error terms. At *t = 23.5 sec*, the feedback part of the loop is turned on to compensate for the ACS drift, without correcting the high frequency jitter. Finally, at *t = 39 sec*, the feedforward portion of the loop

is turned on to correct the high frequency jitter as well. For this plot the feedforward gain was low to showcase the converging of the feedforward correction loop.

Figures 17 and 18 show a more descriptive frequency domain view of LOWFS performance. Figure 17 demonstrates the case of maximum 14 mas slow ACS error combined with worst (top row) and "benign" cases (bottom row) of Cycle 5 jitter. Figure 18 shows the loop performance with 4 mas Cycle 5 ACS jitter and 14 mas tonal error at 10 Hz and 40 Hz. In all scenarios, closing the loop reduced the total LoS error from more than 14 mas to ~0.5 mas under the most unfavorable conditions and <0.3 mas in the typical favorable conditions. This level of residual jitter will allow the WFIRST coronagraph to achieve its optimal performance. It should be noted that noise contributions above ~150 Hz are dominated by the environmental sources described in Table 3, which will be reduced in the next testbed and are in many cases entirely irrelevant for the flight performance. For this reason, we have not included the noise above 150 Hz in the calculations of the residual pointing error.

Finally, figure 19 compares the loop error rejection model prediction and testbed performance, demonstrating their excellent agreement.
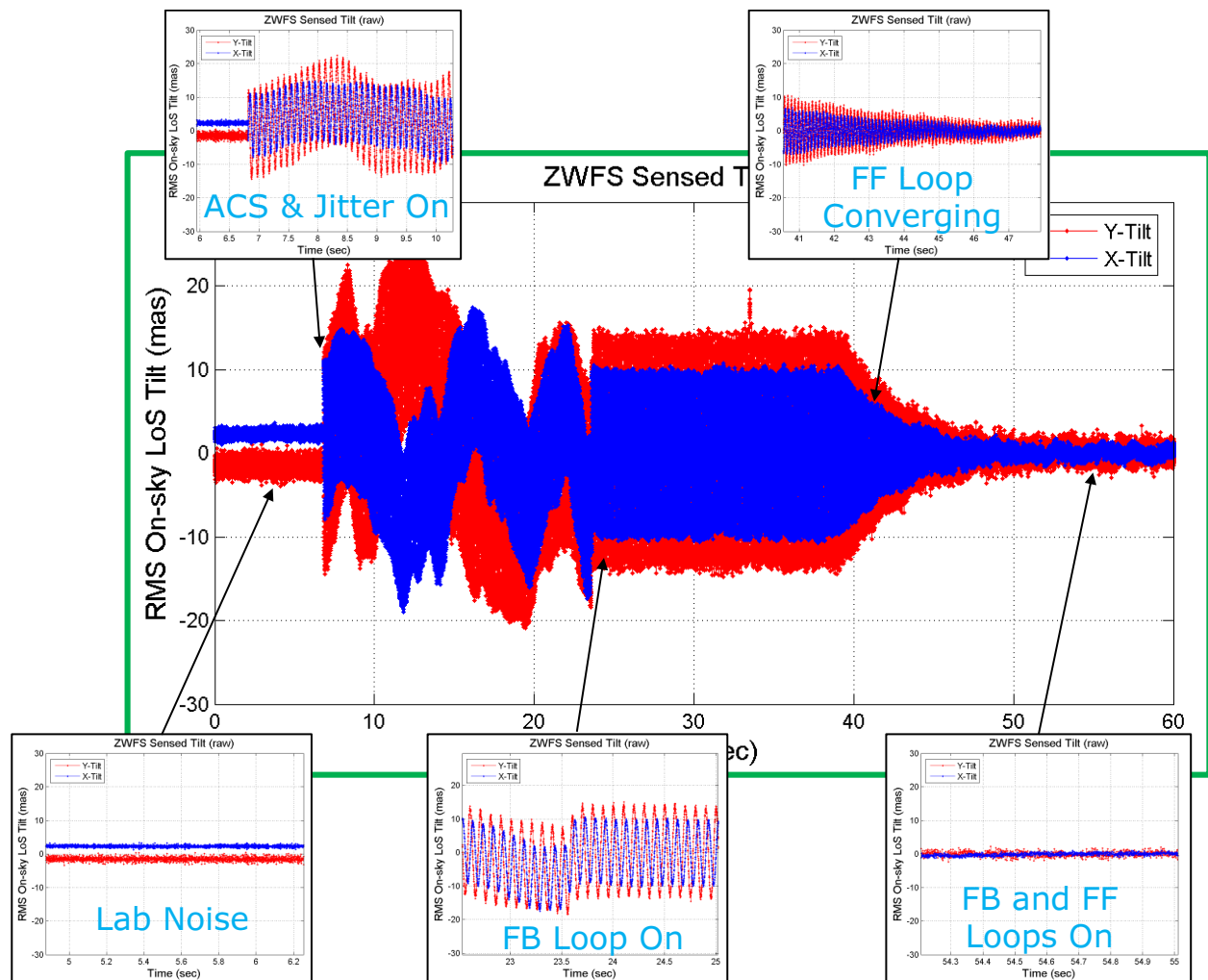
Fig 16. Time domain view of LOWFS/C performance, showing the intervals with lab noise only, uncompensated ACS and jitter error, ACS error correction only via the feedback loop, and correction of both ACS errors and jitter with feedback and feedforward loops on. Small sub-plot panels are showing the time zoomed-in plots for details. The two color traces showing both the X and Y tilts. The tilts have been converted to the equivalent WFIRST on-sky angle using the calibrations.
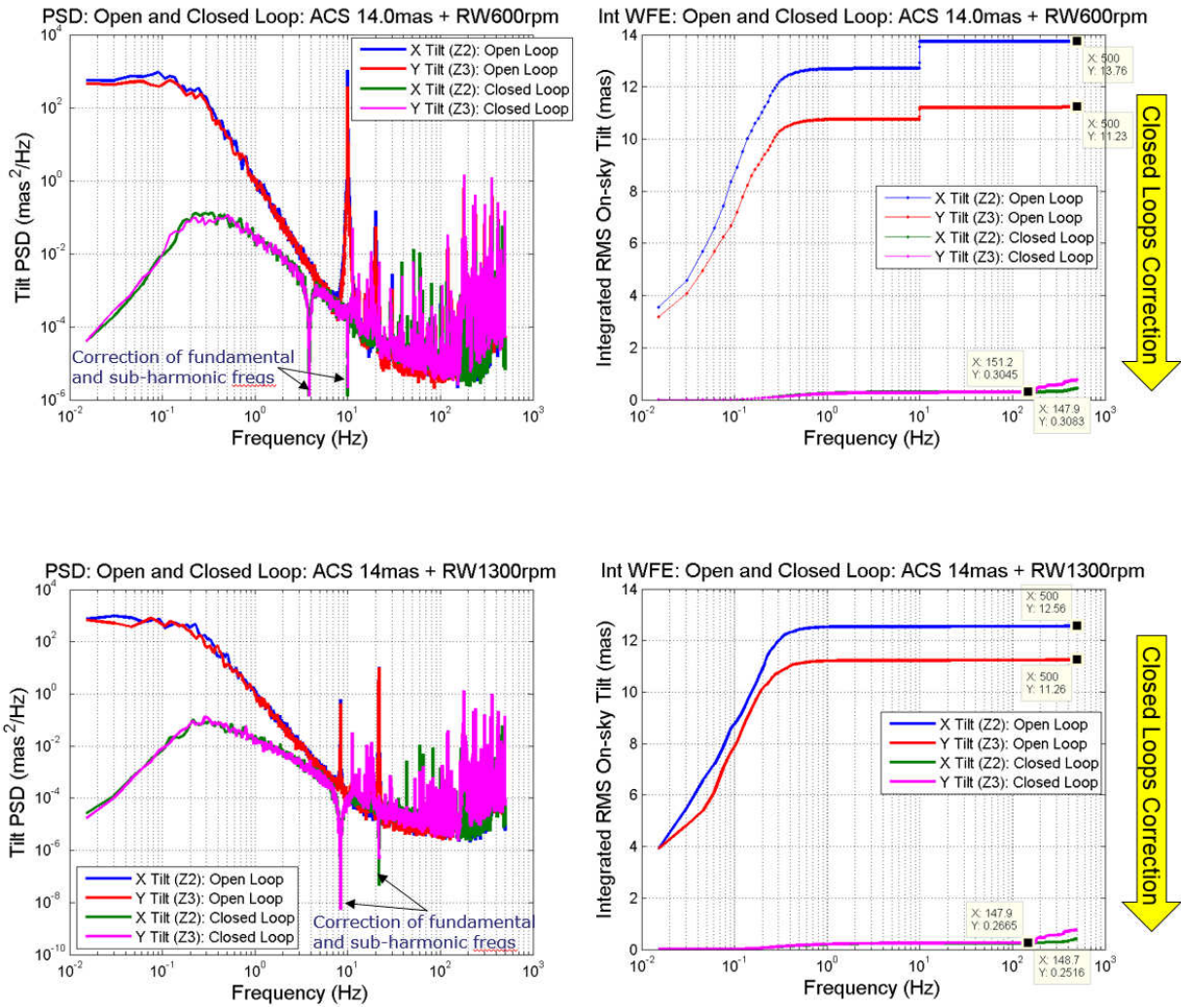
Fig 17. Frequency domain plots of LOWFS/C performance, comparing open loop and closed loop tip and tilt. PSDs are plotted in the left column and integrated RMS tilts are plotted in the right column. The top row shows the case of ACS error scaled up to 14 mas and the jitter corresponding to Cycle 5 estimate for worst-case RWA speed of 600 rpm (10 Hz). The bottom row shows the case of ACS scaled up to 14 mas and jitter corresponding to Cycle 5 estimate for a "benign" RWA speed of 1300 rpm (21.7 Hz). Unlike the 600 rpm case, the RWA induced the jitters at wheel speed of 1300 rpm (21.7 Hz) are much smaller and causes barely visible steps at 21.7 Hz in the forward integrated plots (lower right.)
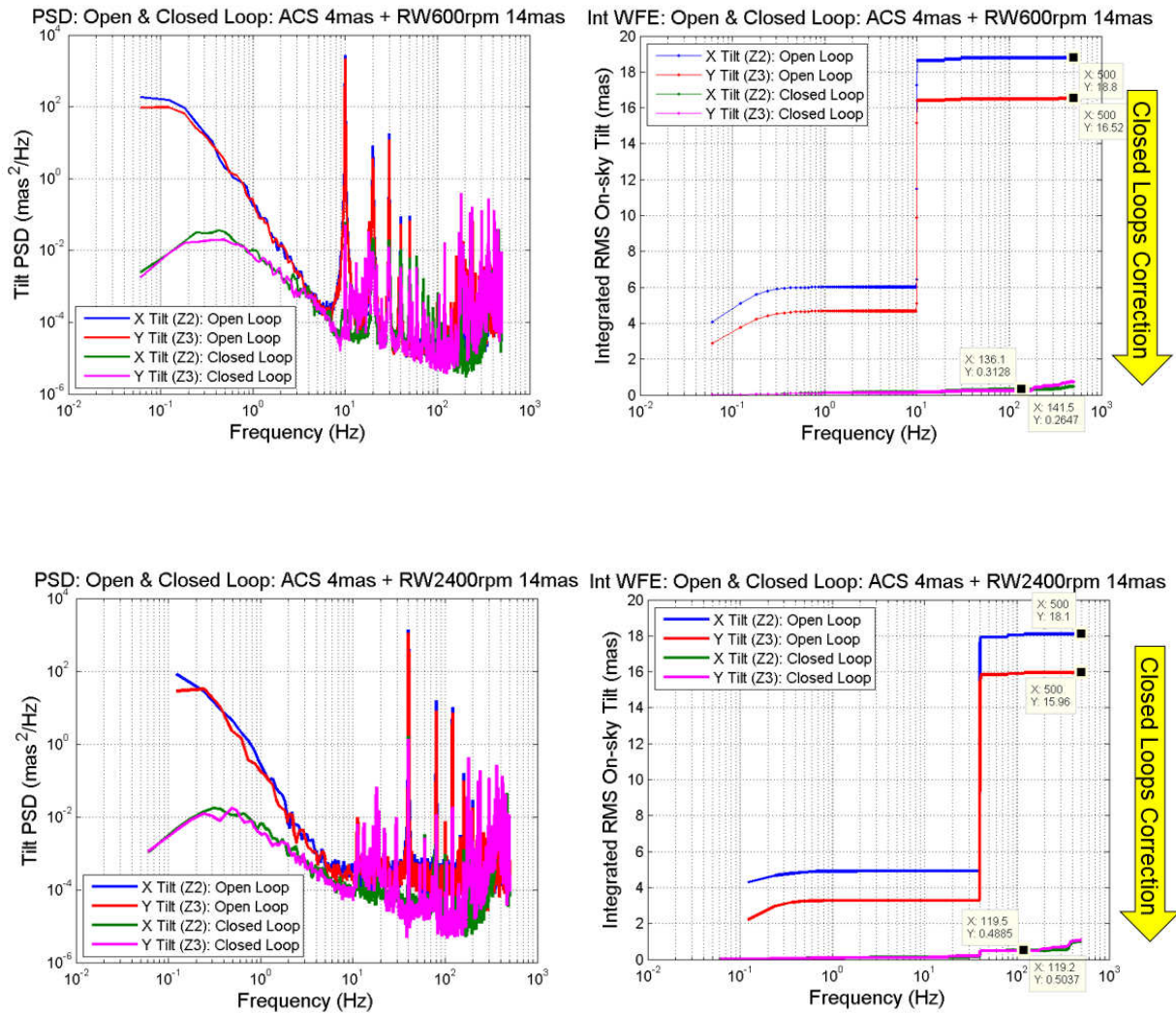
Fig 18. Frequency domain plots of LOWFS/C performance, comparing open loop and closed loop tip and tilt. PSDs are plotted in the left column and integrated RMS tilts are plotted in the right column. The top row shows the case of 4 mas ACS error and a single-tune 14 mas rms jitter at RWA wheel speed of 600 rpm (10 Hz.) The bottom row shows the case of 4 mas ACS error and tonal 14 mas rms jitter at wheel speed of 2400 rpm (40 Hz.)
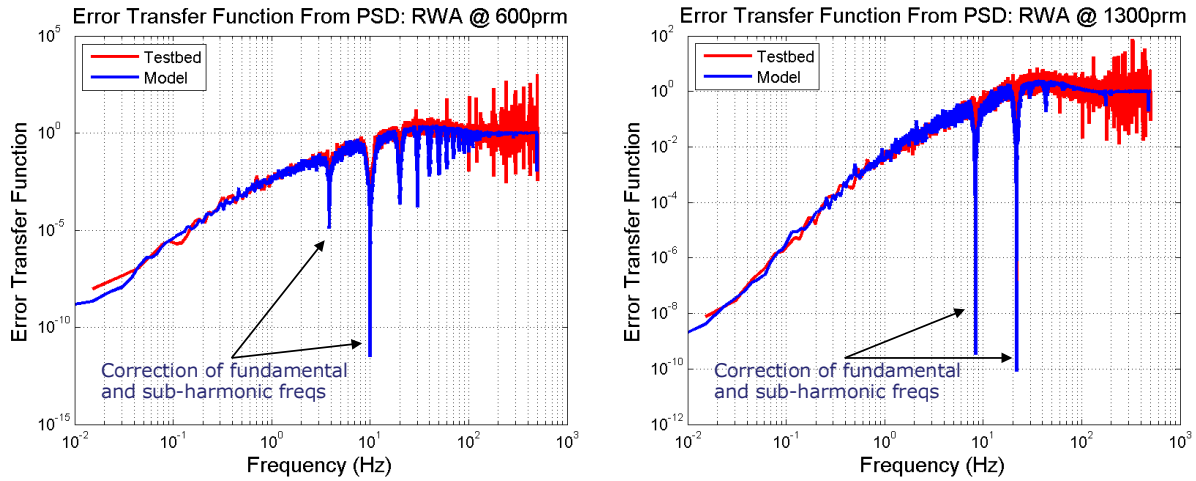
Fig 19. The comparison of error transfer function model predictions and experimental results for the cases corresponding to 600 rpm (left) and 1300 rpm (right). The error transfer functions are calculated by dividing the closed loop LoS residual by the input disturbance. Please noted the excessive noise at the higher frequency (> 100 Hz) in testbed data is due to the lab environment.

5   CONCLUSION

WFIRST coronagraph requires a low order wavefront sensing and control subsystem to enable the instrument to reach high contrast and to maintain contrast stability. This LOWFS/C subsystem uses the Zernike phase contrast wavefront sensor, which is combined with the coronagraph's focal plane mask, to sense the low order wavefront drift and line-of-sight jitter using the rejected starlight. Using the differential image as the signal, the ZWFS can provide the sensitivity needed to sense and correct the expected WFIRST LoS jitter and wavefront drift. Simulations of LOWFS/C closed loop jitter suppression and low order WFE correction have been done for the realistic disturbances generated by the current observatory models and on-orbit operating scenarios. A LOWFS/C testbed including the OTA Simulator has been built to produce the expected WFIRST-AFTA telescope LoS jitter and wavefront drift and perform stand-alone testing of the LOWFS/C subsystem prior to its integration with the coronagraph. The test results have shown excellent agreement with the model predictions. Low order wavefront error sensing <0.2 mas for tip and tilt and <0.25 nm for focus have been demonstrated. Closed loop control that brings LoS error residuals to ~0.3 mas rms per axis for favorable reaction wheel speeds that are typical in the planned RWA operational range, and to ~0.5 mas rms per axis for the worst-case RWA speeds was shown. LOWFS/C performance modes that could not be addressed in the stand-alone testbed were extensively modeled and will be tested in the dynamic occulting mask coronagraph testbed during 2016.

ACKNOWLEDGMENTS

ACRONYMS

ACS: Attitude Control System

AFTA: Astrophysics-Focused Space Telescope Assets

CGI: Coronagraphic Instrument

DM: Deformable Mirror

EFC: Electric Field Conjugation

FSM: Fast Steering Mirror

HCIT: High Contrast Imaging Testbed

HLC: Hybrid Lyot Coronagraph

JM: Jitter Mirror

LOWFS/C: Low Order Wavefront Sensing and Control

LoS: Line of Sight

NASA: National Aeronautics and Space Administration

OAP: Off-Axis Parabola

OMC: Occulting Mask Coronagraph

OTA: Optical Telescope Assembly

PSD: Power Spectral Density

PSF: Point Spread Function

RMS: Root Mean Square

RWA: Reaction Wheel Assembly

SPC: Shape Pupil Coronagraph

TAC: Technical Analysis Committee

WFC: Wavefront Control

WFE: Wavefront Error

WFIRST: Wide-Field Infrared Survey Telescope

REFERENCES

[1] "WFIRST cycle 5 closeout jitter," Internal communication (2015).
[2] J. Krist, B. Nemati, H. Zhou, E. Sidick, "An overview of WFIRST/AFTA coronagraph optical modeling", Proc. SPIE 9605, pp. 9605-4, (2015).
[3] J. Krist, B. Nemati, B. Mennesson, "Numerical modelling of the proposed WFIRST-AFTA coronagraphs and their predicted performances", submitted to JATIS, (2015).
[4] A. Give'on, B. Kern, S. Shaklan, D. Moody, L. Pueyo, "Broadband wavefront correction algorithm for high-contrast imaging system," Proc. SPIE, 6691, 66910A (2007).
[5] K. Zernike, MNRAS, 94, 377 (1934)
[6] J. K. Wallace, S. Rao, R. M. Jensen-Clem, G. Serabyn, "Phase-Shifting Zernike Interferometer Wavefront Sensor", Proc. SPIE 8126, 81260F-1 (2011)

[7] F. Shi, K. Balasubramanian, R. Hein, R. Lam, D. Moore, J. Moore, K. Patterson, I. Poberezhskiy, J. Shields, E. Sidick, H. Tang, T. Truong, J. K. Wallace, X. Wang, D. Wilson, "Low Order Wavefront Sensing and Control for WFIRST-AFTA Coronagraph", submitted to JATIS, (2015).

[8] R. Demers, F. G. Dekens, R. J. Calvet, Z. Chang, R. T. Effinger, E. M. Ek, L. Jones, A. Loc, B. Nemati, C. Noecker, T. Neville, H. Pham, H. Tang, J. Villalvazo, "Requirements and design reference mission for the WFIRST-AFTA coronagraph instrument", Proc. SPIE 9605, pp. 9605-1 (2015).

[9] K. Balasubramanian, V. White, K. Yee, P. Echternach, R. Muller, M. Dickie, E. Cady, D. Ryan, I. Poberezhskiy, H. Zhao, B. Kern, J. Krist, B. Nemati, K. Patterson, A.J. Riggs, N. Zimmerman, and N. J. Kasdin, "WFIRST-AFTA coronagraph shaped pupil masks: Design, Fabrication and Characterization", submitted to JATIS, (2015).

[10] J. Trauger, B. Gordon, J. Krist, D. Moody, "Hybrid Lyot Coronagraph for WFIRST-AFTA: coronagraph design and performance metrics", submitted to JATIS, (2015).

[11] X. Wang, J. K. Wallace, F. Shi, "Zernike wavefront sensor (ZWFS) modeling development for low order wavefront sensing (LOWFS) on wide-field IR space telescope (WFIRST) / astrophysics focused telescope assets (AFTA)", Proc. SPIE 9605, pp. 9605-79, (2015).

[12] A. Toorian, R. Smythe, M. Morles, J. Carson, J. Moore, "Flight qualification and performance testing of SIM precision optical mechanisms", Proc. SPIE 7734 (2010).

[13] K. Patterson, J. Shields, X. Wang, H. Tang, A. Azizi, P. Brugarolas, M. Mandic, and F. Shi, "Control Design for Momentum-Compensated Fast Steering Mirror for the WFIRST-AFTA Coronagraph Instrument", Proc. SPIE 9605, pp. 9605-83, (2015).

[14] Erkin Sidick, and F. Shi, "Effect of DM actuator gain errors on the WFIRST/AFTA coronagraph contrast performance", Proc. SPIE 9605, pp. 9505-5, (2015).